Autocorrelation artifacts in optical coherence tomography and interferometric synthetic aperture microscopy

Brynmor J. Davis, Tyler S. Ralston, Daniel L. Marks, Stephen A. Boppart, and P. Scott Carney*

Beckman Institute for Advanced Science and Technology and the Department of Electrical and Computer Engineering, University of Illinois at Urbana-Champaign, 405 North Mathews Avenue, Urbana, Illinois 61801, USA
**Corresponding author: carney@uiuc.edu*

Received January 4, 2007; revised March 14, 2007; accepted March 28, 2007; posted April 2, 2007 (Doc. ID 78719); published May 1, 2007

Interferometric synthetic aperture microscopy processing of optical coherence tomography data has been shown to allow computational focusing of *en face* planes that have traditionally been regarded as out of focus. It is shown that this focusing of the image also produces a defocusing effect in autocorrelation artifacts resulting from Fourier-domain data collection. This effect is verified experimentally and through simulation.

OCIS codes: 100.3190, 100.6890, 170.1650, 170.4500, 110.6880, 180.3170.

Spectral-domain optical coherence tomography (OCT) [1] has significant signal-to-noise and speed advantages over time-domain OCT [2]. However, the signal gathered by spectral interferometry exhibits conjugate and autocorrelation artifacts that can overlap the desired image of the object structure. Modulation of the reference field [3–6] can distinguish these artifacts at the cost of additional instrumentation. A recent theoretical analysis has also suggested that under certain conditions it may be possible to eliminate autocorrelation artifacts through postprocessing [7].

Interferometric synthetic aperture microscopy (ISAM) [8–11] is a recently developed method based on the solution of the inverse scattering problem for instrumentation similar to OCT but with augmentation to provide phase stability over the data set. ISAM provides spatially uniform resolution of three-dimensional structure, including features that are out of focus in conventional OCT imaging. In this Letter, it is shown that the ISAM algorithm also defocuses the autocorrelation and conjugate image artifacts, mitigating their effects in most cases. This additional benefit is inherent to the ISAM methodology and requires no supplementary instrumentation or signal processing.

In OCT and ISAM a beam of light is projected into a highly scattering sample, and the backscattered light is collected and measured in an interferometer. The center of the beam, in a plane perpendicular to the beam axis, is denoted by the position vector $\mathbf{r}_\parallel$. In time-domain OCT, data, I_T, are obtained as a function of the reference delay, τ, and $\mathbf{r}_\parallel$. The measured data are given by the intensity of the sum of a reference field, E_r, and the field scattered from the sample, E_s, and may be written as

$$I_T(\mathbf{r}_\parallel,\tau)=R_{rr}(0)+R_{ss}(\mathbf{r}_\parallel,0)+R_{sr}(\mathbf{r}_\parallel,\tau)+R_{sr}^*(\mathbf{r}_\parallel,\tau), \tag{1}$$

where $R_{ab}(\mathbf{r}_\parallel,\tau)=\langle E_a(\mathbf{r}_\parallel,t)E_b^*(\mathbf{r}_\parallel,t-\tau)\rangle$ and $\langle\ \rangle$ denotes an average over time. The R_{rr} and R_{ss} terms form a constant (in τ) background that can be removed with little difficulty.

In spectral-domain OCT the reference delay is fixed to τ_0, eliminating the need for a moving delay arm, and measurements are taken with spectroscopic sensitivity. Assuming ergodicity, the spectral domain data can then be expressed as

$$\hat{I}_F(\mathbf{r}_\parallel,\omega)=S_{rr}(\omega)+S_{ss}(\mathbf{r}_\parallel,\omega)+e^{i\omega\tau_0}S_{sr}(\mathbf{r}_\parallel,\omega)+e^{-i\omega\tau_0}S_{sr}^*(\mathbf{r}_\parallel,\omega), \tag{2}$$

where $S_{ab}(\mathbf{r}_\parallel,\omega)=(2\pi)^{-1/2}\int R_{ab}(\mathbf{r}_\parallel,\tau)e^{-i\omega\tau}\mathrm{d}\tau$. The inverse Fourier transform of $\hat{I}_F$ brings the data back into the temporal domain,

$$I_F(\mathbf{r}_\parallel,\tau)=R_{rr}(\tau)+R_{ss}(\mathbf{r}_\parallel,\tau)+R_{sr}(\mathbf{r}_\parallel,\tau+\tau_0)+R_{sr}^*(\mathbf{r}_\parallel,-\tau-\tau_0). \tag{3}$$

This equation is complicated by terms not present in the time-domain case shown in Eq. (1). R_{ss} and R_{rr} appear here as functions of τ, and a conjugate image R_{sr}^* is present with an argument distinct from the nonconjugate term.

The constant (in $\mathbf{r}_\parallel$) reference-intensity term R_{rr} in Eq. (3) may be known *a priori* or may be subtracted in a robust manner [12]. Since the sample will generally have a well-defined boundary, there is a τ_m such that $R_{sr}(\mathbf{r}_\parallel,\tau)=0$ for $\tau\leqslant\tau_m$. Chosing the delay on the reference arm such that $\tau_0<\tau_m$ ensures that the direct and conjugate images lie on separate sides of the $\tau=0$ plane. Setting the signal to zero in the conjugate image region ($\tau<0$) is equivalent to application of the Hilbert transform in the frequency domain [13]. Since the autocorrelation is centered at the origin ($\tau=0$), a scheme of further decreasing τ_0 might be expected to result in a separation of the image and the autocorrelation [14]. However, this does not happen until the offset has been further increased by an amount corresponding to the optical thickness of the sample, not a practical option in most cases. Such an approach results in an effective loss of imaging range

and decreased performance in the spectrometer [2].

In this Letter it is assumed that a single measurement is taken with τ_0 set such that the real and conjugate images can just be separated. A quantitative estimate of the object is made from these data using both OCT and ISAM, and the resulting autocorrelation artifacts are investigated.

The signal $S(\mathbf{r}_\parallel,k)=S_{sr}(\mathbf{r}_\parallel,kc/n)$ can be defined by changing from temporal to spatial spectra according to the dispersion relation $k=n\omega/c$. In samples with spectrally varying background properties, a more complex relation can be employed and dispersion compensated digitally [10,15]. Autocorrelation and conjugate image artifacts arise because S_{sr} is not directly available, and S is therefore calculated from the data I_F.

By taking the two-dimensional Fourier transform of S (indicated by a tilde) with respect to $\mathbf{r}_\parallel$, the most general ISAM model [11] can be written as

$$\tilde{S}(\mathbf{Q}_\parallel,k)=\int \tilde{L}(\mathbf{Q}_\parallel,k,z)e^{i2k_z z}\tilde{\eta}(\mathbf{Q}_\parallel,z)\mathrm{d}z, \qquad (4)$$

where $k_z=(k^2-Q_\parallel^2)^{0.5}$ is the axial component of the wave vector, η is the object susceptibility, and $\tilde{L}$ is determined by the specific instrumentation used. When the z dependence in the factor $\tilde{L}$ is neglected and it is assumed that $k_z=k$ (an extreme form of the paraxial approximation), the conventional OCT model is recovered in which the transverse and axial effects are decoupled. That is, OCT reconstruction may be implemented by an inverse Fourier transform of S over k and a scaling of the z axis.

It has been shown that Eq. (4) can be inverted, that is, the inverse scattering problem may be solved, by Fourier resampling and linear filtering [8–11]. The coherent nature of the data allows the scattered field, not the scattered intensity, to be addressed directly and thus allows computational refocusing at all axial positions. Consequently, the spatial effects of ISAM vary with the axial distance from the focal plane. Spatially invariant resolution is achieved from data obtained with a fixed focal plane, regardless of the numerical aperture.

Since the ISAM processing is designed to refocus the data only in the R_{sr} term, it can be expected to defocus the shifted data in the conjugate and autocorrelation terms. An example of this effect can be seen in Fig. 1. The object shown is defined on a three-dimensional grid with 2 μm spacing in $\mathbf{r}_\parallel$ and 4 μm spacing in z. The object lies in a 1 mm$\times$300 μm $\times$2 mm volume and consists of spherical shells of radii 700 μm (only partially visible) and 40 μm and 30 point scatterers in the x–z plane, one of which lies on the interieror of the smaller sphere. The spherical shells are described by $\eta(\mathbf{r})=\eta_0\delta^{(1)}(|\mathbf{r}-\mathbf{r}_p|-a)$, where a is the radius, $\mathbf{r}_p$ determines the structure's location, $\delta^{(1)}$ is the one-dimensional delta function, and η_0 represents an arbitrary unit of contrast from the background of zero susceptibility ($n=1$). The point scatterers are described by $\eta(\mathbf{r})=10\eta_0\delta^{(3)}(\mathbf{r}-\mathbf{r}_p)$. The data were synthesized at 600 wavelengths between 780 and 820 nm by using a lens with numerical aperture of 0.05. The transverse dimension $\mathbf{r}_\parallel$ was sampled on a 4 μm grid over a 800 μm$\times$200 μm area, and the data were generated by using a full vectorial model [11] with the assumption of isotropic scattering.

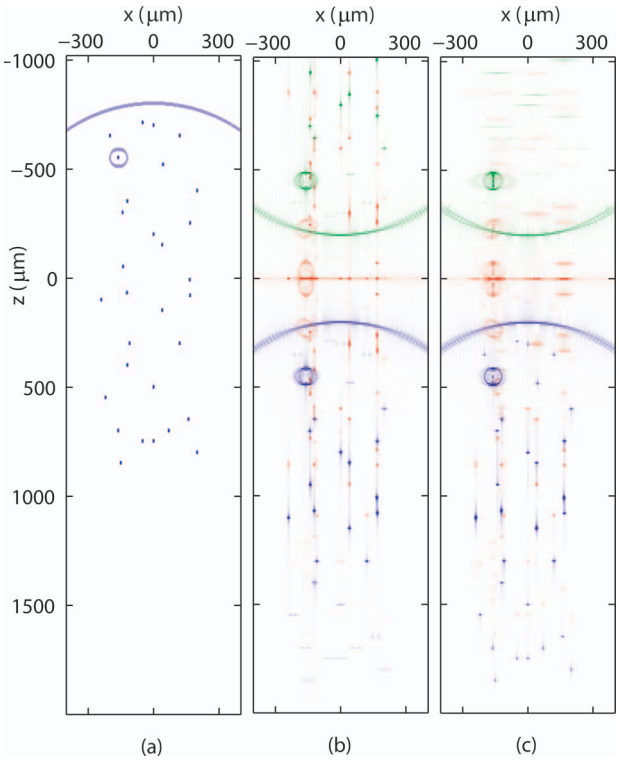

Fig. 1. (a) The x–z plane of the object and (b) the resulting OCT and (c) ISAM images with $c\tau_0=-1$ mm. The structures in (a) have been broadened for display. In (b) and (c) the contribution of R_{sr} is shown in blue, R_{sr}^* (conjugate image) in green, and R_{ss} (autocorrelation) in red. The color scale is clipped at 10% of the maximum signal so that low-level detail can be seen.

These simulations show the effects of OCT and ISAM processing. When $\tau_0=0$, the $z=0$ plane is at the focal plane of the lens; however, these simulations use $c\tau_0=-1$ mm so that the data terms separate spatially. The R_{rr} term is assumed to have been perfectly removed, and the strength of the reference field is adjusted so that the contributing terms are visible on the same scale. The ISAM algorithm used consists only of the appropriate Fourier-domain resampling.

The simulation results confirm that ISAM refocuses points that are out of focus in the traditional OCT reconstruction and produces defocus in the conjugate and autocorrelation images. As the distance from focus or the numerical aperture is increased, the defocus in the autocorrelation is increased. Conversely, autocorrelation artifacts near the focal plane are not blurred, as ISAM does not produce significant change in regions that are already in focus.

The defocus of the autocorrelation term can also be seen experimentally as shown in Fig. 2. A sample consisting of beads of titanium dioxide, with an average diameter of 1 μm, embedded in a background of silicone is imaged. A 0.05 numerical aperture (NA) lens is used to collect wavelengths between 750 and 850 nm. The instrument used is that described in an

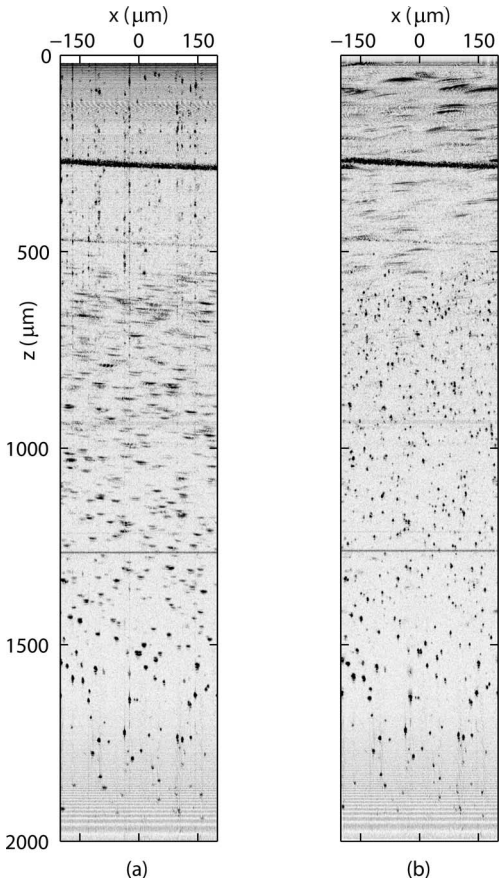

Fig. 2. (a) OCT and (b) ISAM reconstructions from real data. The gray scale is clipped at 10% of the maximum value so that low-level detail can be seen.

earlier demonstration of ISAM [10]. The focus lies at approximately 1750 μm, the reference plane is $z=0$, and a glass coverslip extends from approximately 300 to 600 μm. The OCT reconstruction shows point scatterers near the focus, defocus away from that, and a strong autocorrelation effect above the sample and in the coverslip where no signal should, in principle, be seen. When ISAM is applied, the scatterers within the sample are bought into focus, and the autocorrelation artifacts are defocused.

In ISAM, computational focusing of the image, as well as the corresponding defocus of the autocorrelation, is implemented by using resampling in the Fourier domain. This coordinate warping generally produces only a small change in the integrated square magnitude of S_{ss} and S_{sr}. Consequently the energies in the image and autocorrelation contributions are not significantly different than in OCT. The autocorrelation mitigation shown here relies on the desired image being focused while the autocorrelation is blurred, with a corresponding drop in peak amplitude. In a very dense sample the blurred autocorrelation features may overlap and add, resulting in little improvement. Indeed, since the ISAM approach produces coherent defocus of the artifacts, it is possible that in a sample with dense structure the defocused features of the autocorrelation may interfere with each other to produce new sharp features. The beginning of such a phenomenon may be seen at the top of Fig. 2(b) and in Fig. 1(c) near $z=0$, where in a few places fringes are seen to emerge in the overlap of defocused points of autocorrelation.

The simulations and experiments shown here have been chosen to be well within the range of focusing parameters used in OCT today. ISAM obviates the trade between depth of focus and resolution and so enables the use of much higher NA optics without loss of depth of imaging. The artifact defocusing seen here becomes more pronounced as the NA is increased. This suggests that future implementations of spectral-domain ISAM may find further autocorrelation advantage by using high-NA lenses with the geometrical focus shifted away from the region of interest.

This work was supported in part by the National Institutes of Health (NIBIB, Roadmap Initiative, 1 R21 EB005321, to S. A. Boppart) and the National Science Foundation (BES 05-19920, to S. A. Boppart, and CAREER Award, 0239265, to P. S. Carney).

References

1. A. F. Fercher, C. K. Hitzenberger, G. Kamp, and S. Y. El-Zaiat, Opt. Commun. **117**, 43 (1995).
2. R. Leitgeb, C. Hitzenberger, and A. Fercher, Opt. Express **11**, 889 (2003).
3. R. A. Leitgeb, C. K. Hitzenberger, A. F. Fercher, and T. Bajraszewski, Opt. Lett. **28**, 2201 (2003).
4. J. Zhang, J. S. Nelson, and Z. Chen, Opt. Lett. **30**, 147 (2005).
5. M. Sarunic, M. A. Choma, C. Yang, and J. A. Izatt, Opt. Express **13**, 957 (2005).
6. J. Ai and L. V. Wang, Appl. Phys. Lett. **88**, 111115 (2006).
7. A. Ozcan, M. J. F. Digonnet, and G. S. Kino, J. Opt. Soc. Am. A **23**, 1669 (2006).
8. T. S. Ralston, D. L. Marks, P. S. Carney, and S. A. Boppart, J. Opt. Soc. Am. A **23**, 1027 (2006).
9. T. S. Ralston, D. L. Marks, S. A. Boppart, and P. S. Carney, Opt. Lett. **31**, 3585 (2006).
10. T. S. Ralston, D. L. Marks, P. S. Carney, and S. A. Boppart, Nat. Phys. **3**, 129 (2007).
11. B. J. Davis, S. C. Schlachter, D. L. Marks, T. S. Ralston, S. A. Boppart, and P. S. Carney, "Nonparaxial vector-field modeling of optical coherence tomography and interferometric synthetic aperture microscopy," J. Opt. Soc. Am. A (in press).
12. R. K. Wang and Z. Ma, Phys. Med. Biol. **51**, 3231 (2006).
13. Y. Zhao, Z. Chen, C. Saxer, S. Xiang, J. F. de Boer, and J. S. Nelson, Opt. Lett. **25**, 114 (2000).
14. P. Andretzky, M. Knauer, F. Kiesewetter, and G. Häusler, Proc. SPIE **3915**, 55 (2000).
15. D. L. Marks, A. L. Oldenburg, J. J. Reynolds, and S. A. Boppart, Appl. Opt. **42**, 204 (2003).